Transient chirality inversion during racemization of a helical cobalt(III) complex

Yoko Sakata[a,b], Shunsuke Chiba[a], and Shigehisa Akine[a,b,1]

[a]Graduate School of Natural Science and Technology, Kanazawa University, Kanazawa 920-1192, Japan; and [b]Nano Life Science Institute, Kanazawa University, Kanazawa 920-1192, Japan

Edited by Joel Yuen-Zhou, University of California San Diego, La Jolla, CA; received August 26, 2021; accepted January 7, 2022 by Editorial Board Member Shaul Mukamel

While most responsive molecules show a trivial first-order exponential relaxation upon stimulation, increasing interest has recently focused on unusual nontrivial time responses such as chemical clocks and chemical oscillators. These unique time profiles principally originate from complicated multistep reactions involving an autocatalytic redox process of small inorganic species such as BrO_3^- or from supramolecular assembling of organic molecules. In this study, we have found that a very unusual time response was observed in a unimolecular platform just by integrating multiple reaction centers in a molecule. A triple-helical metallocryptand, $[LCo_3A_6]^{3+}$ (A = (*S*)-1-phenylethylamine), underwent a transient chirality inversion from *P*-rich (right-handed) to *M*-rich (left-handed) then racemic during the racemization driven by the multistep ligand exchange with piperidine. In contrast, the reverse reaction showed a simple monotonic change with an induction time without showing the transient chirality inversion. Consequently, the *M* helicity appeared only in the forward reaction. Detailed mass spectrometric analysis suggested that the forward and reverse reactions proceeded in different pathways to make a unique hysteretic cycle.

chirality inversion | nonlinear kinetics | helical structure | ligand exchange | hysteretic cycle

Responsive molecules play a central role in both artificial and biological functional systems (1–5). They change their molecular structure by a physical or chemical stimulus to enable subsequent functions such as signal transduction. In general, fast response has been believed to be desirable so that the next molecular functions can quickly start to work. The time profiles of the response can usually be described as a (pseudo–) first-order exponential relaxation (Fig. 1 *A*, *i*), which gives a simple monotonic change from the initial to the final values in the molecular functions or properties.

In contrast, there are reactions that show an unusual time response, which is far from the trivial first-order kinetics. These include chemical clocks (Fig. 1 *A*, *ii*) (6, 7) and chemical oscillators (Fig. 1 *A*, *iii*) (8–12), which are known as thermodynamically open systems (13). The unique oscillating time profiles are observed only in limited systems, although oscillation is quite a ubiquitous physical phenomenon in classical/quantum mechanics, electromagnetism, etc. The chemical oscillation originates from very complicated multistep reactions involving autocatalytic redox processes of simple inorganic species, such as the BrO_3^- ion (8–13), and this has been successfully utilized to develop oscillating materials (14–19) that enable periodic changes in various kinds of molecular functions, physical properties, or chemical reactivities upon stimulation.

Recently, unique time responses have also been observed in some dissipative supramolecular assemblies (20–25), in which their physical quantity shows one increase–decrease cycle each time a chemical fuel is added (26–30) or multiple increase–decrease cycles (31, 32). More simply, formation of self-assembled structures from small organic molecules sometimes exhibits unique nonlinear time responses with a significant lag time mainly due to the pathway complexity (33, 34). Typically, the constituent molecules first form a metastable assembly (35–42) or a kinetically trapped state prior to the assembly (43–46), which is then converted into the most thermodynamically stable state after a substantial lag time. This two-phase time course change sometimes leads to a chirality inversion with time; i.e., the right-handed helical aggregate is initially formed, but this is converted into the left-handed helical form at a later time (47–51). This observation is noteworthy because the time-dependent positive/negative inversion is one of the important features of oscillation in physical phenomena. In principle, however, these unique nonlinear time responses have been observed mostly during the formation of supramolecular polymers but not in a unimolecular system.

In this study, we have found that an unprecedented nonlinear time response with a transient chirality inversion was observed in a unimolecular system just by integrating multiple reaction centers in a triple-helical molecular scaffold; i.e., a helical cobalt(III) metallocryptand underwent a racemization with a transient chirality inversion. Racemization is a ubiquitous chemical conversion from an optically active compound to the corresponding racemic mixture (Fig. 1*B*). Principally, racemization is a unimolecular reaction that shows a very normal time profile described as the first-order exponential relaxation (Fig. 1 *A*, *iv*). However, if racemization is driven by a multistep reaction, the time response could be nonlinear. Indeed, the

Significance

We first observed a transient chirality inversion on a simple unimolecular platform during the racemization of a chiral helical complex $[LCo_3A_6]^{3+}$, i.e., the helicity changed from *P*-rich (right-handed) to *M*-rich (left-handed), which then racemized to a *P*/*M* equimolar mixture in spite of the absence of a reagent that could induce the *M* helix. This transient chirality inversion was observed only in the forward reaction, whereas the reverse reaction showed a simple monotonic change with an induction time. Consequently, the *M* helicity appeared only in the forward reaction. These forward and reverse reactions constitute a hysteretic cycle. Compounds showing such unique time responses would be useful for developing time-programmable switchable materials that can control the physical/chemical properties in a time-dependent manner.

Author contributions: Y.S. and S.A. designed research; Y.S. and S.C. performed research; Y.S., S.C., and S.A. analyzed data; and Y.S. and S.A. wrote the paper.

The authors declare no competing interest.

This article is a PNAS Direct Submission. J.Y.-Z. is a guest editor invited by the Editorial Board.

[1]To whom correspondence may be addressed. Email: akine@se.kanazawa-u.ac.jp.

This article contains supporting information online at http://www.pnas.org/lookup/suppl/doi:10.1073/pnas.2113237119/-/DCSupplemental.

Published March 8, 2022.

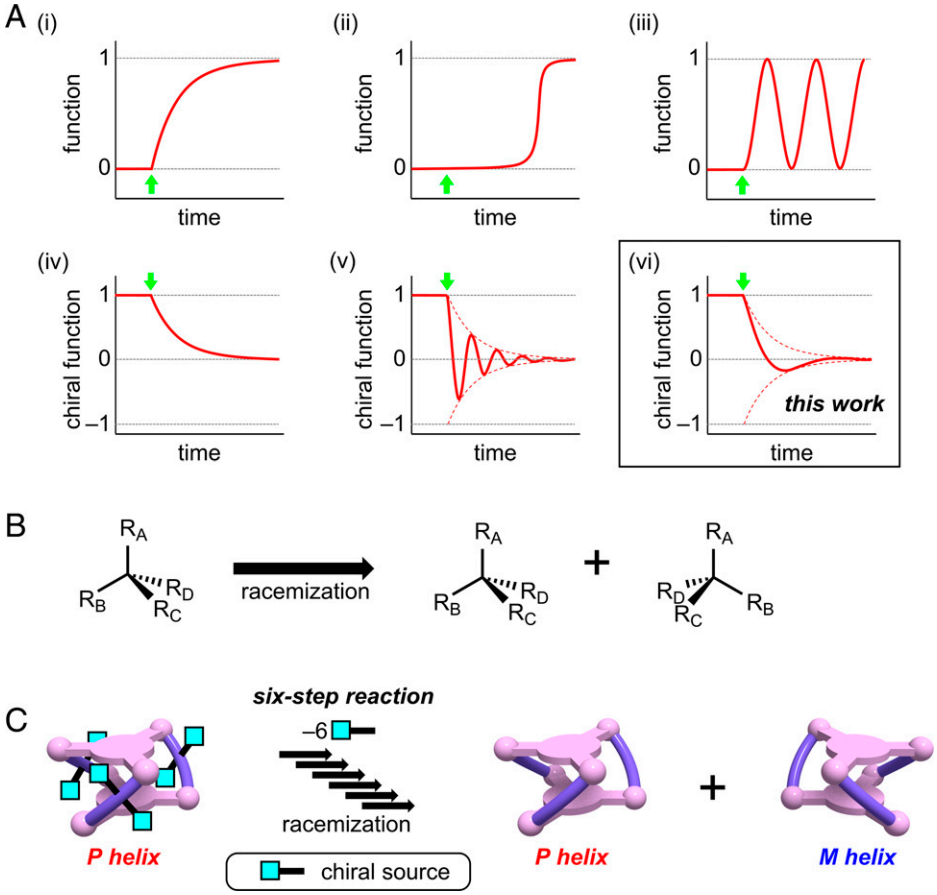

Fig. 1. Time response of functional molecules. (*A*) Various types of response curves upon stimulation (green arrows): (*i*) exponential decay, (*ii*) time response in a chemical clock, (*iii*) time response in a chemical oscillator, (*iv*) normal time response in racemization, and (*v* and *vi*) transient chirality inversion during racemization. (*B*) Racemization of a chiral carbon compound via a single-step reaction. (*C*) Racemization of a helical molecule via a six-step reaction.

cobalt complexes $[LCo_3X_6]^{3+}$ (Scheme 1) in this study showed quite an unusual time response with a transient chirality inversion (Fig. 1 *A*, *v* and *vi*) due to the multistep reaction when all six chiral ligands, **A** (=(*S*)-1-phenylethylamine), were replaced by an achiral ligand in a multistep manner (Fig. 1*C*). In addition, a unique hysteretic cycle was achieved thanks to this transient chirality inversion, which was not observed in the reverse reaction.

Results and Discussion

Transient Chirality Inversion Driven by the Ligand Exchange. As a platform for nontrivial time course changes driven by a multistep transformation, we used our triple-helical complex, $[LCo_3X_6]^{3+}$ (52–54), which has six exchangeable sites to allow six-step reactions. This complex has a dynamic helical structure, whose right- and left-handed forms (*P* and *M* forms, respectively, hereafter) are in slow equilibrium on the timescale of minutes to hours. The *P*/*M* ratios of the $[LCo_3X_6]^{3+}$ helix can be shifted by the introduction of a chiral ligand at the six exchangeable sites (Scheme 1) (54) because each of the three hexacoordinate cobalt(III) centers can undergo ligand exchange at the two axial sites (55–59). This means that $[LCo_3X_6]^{3+}$ will undergo racemization via a six-step process, if all the chiral ligands X are replaced with achiral ones (Fig. 1*C*).

The helical complex $[LCo_3\mathbf{A}_6](OTf)_3$ was synthesized by the reaction of the corresponding free ligand (60, 61) with cobalt(II) acetate under aerobic conditions in the presence of chiral amine **A** according to our previous report (54). The right-handed helix was dominant in a methanol solution, and the *P*/*M* diastereomeric ratio was 88:12 (*SI Appendix*, Fig. S1). We investigated the sixfold exchange of amine **A** with piperidine in this complex $[LCo_3\mathbf{A}_6](OTf)_3$. This would cause racemization of the *P*-rich $[LCo_3]^{3+}$ triple helix because the *P* and *M* forms become an enantiomer pair after complete removal of the chiral auxiliary **A** (Fig. 1*C* and *SI Appendix*, Fig. S2).

Interestingly, when piperidine (120 equivalents; equiv hereafter) was added to a solution of $[LCo_3\mathbf{A}_6](OTf)_3$ (denoted as **A6** hereafter), the intensity of circular dichroism (CD) showed an unusual time course change instead of the usual monotonic decay of racemization. The negative CD signal at 530 to 550 nm, which is indicative of the *P* helix, immediately decreased and turned positive after 7 min (Fig. 2*A* and *SI Appendix*, Fig. S3). After reaching a maximum after 60 to 120 min, this positive CD signal gradually decreased and became completely silent after 2 d, which implies that the $[LCo_3]^{3+}$ triple helix was finally racemized. Since the sign of the CD signals around 530 to 550 nm directly reflects the *P*/*M* helicity of the $[LCo_3]^{3+}$ triple helix, this time course change represents a transient chirality inversion of the $[LCo_3]^{3+}$ triple helix, i.e., *P*-rich → *M*-rich → racemic as depicted in Fig. 1 *A*, *vi*. When the enantiomeric metallocryptand $[LCo_3\mathbf{A}'_6]^{3+}$ (**A′** = (*R*)-1-phenylethylamine) with the opposite chirality was used as the starting complex, the trace of the time dependence of the CD intensities was almost the perfect mirror image of that for $[LCo_3\mathbf{A}_6]^{3+}$ (*SI Appendix*, Figs. S4 and S5). This again confirmed that the removal of the chiral source, **A** or **A′**, caused the unique transient chirality inversion during the racemization.

It should be noted that the sixfold ligand exchange from $[LCo_3\mathbf{A}_6]^{3+}$ (=**A6**) to $[LCo_3(pip)_6]^{3+}$ (=**A0**) was completed at a

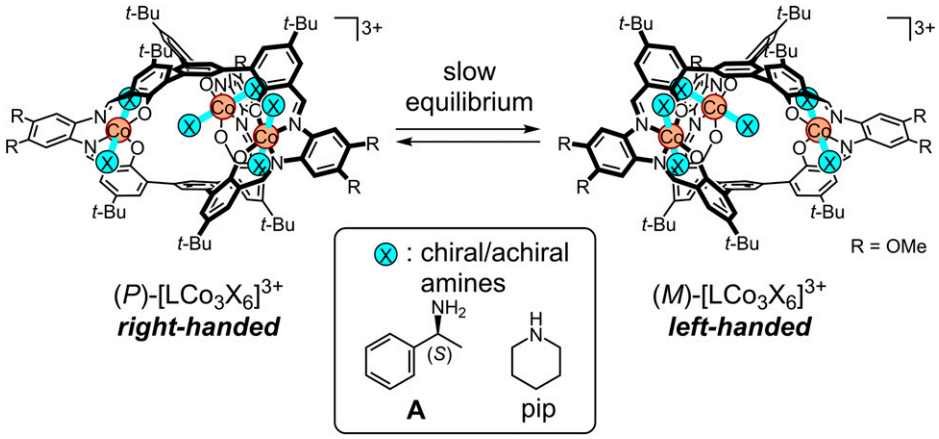

Scheme 1. *P*/*M* helicity inversion of the helical complex $[LCo_3X_6]^{3+}$ (X = **A** or pip).

very early stage (60 to 120 min), although a positive CD signal was still observed with a significant intensity. The electrospray ionization time-of-flight (ESI-TOF) mass spectra (Fig. 2*B* and *SI Appendix*, Fig. S6) and the ^{1}H NMR spectra (*SI Appendix*, Fig. S7) after 60 to 120 min almost exclusively showed the peaks of the fully exchanged product $[LCo_3(pip)_6]^{3+}$ (=**A0**) without showing significant peaks for the intermediate species $[LCo_3\mathbf{A}_n(pip)_{(6-n)}]^{3+}$ (n = 5, 4, 3, 2, and 1; denoted as **A5**, **A4**, **A3**, **A2**, and **A1**, hereafter, using the number of the chiral ligand **A**). Obviously, this unusual time response during the racemization should be ascribed to the multistep ligand exchange at the six available sites as well as the relatively slow *P*/*M* equilibrium shifts of each of the intermediates and the final product.

In order to clarify the mechanism of the unique transient chirality inversion, we carefully analyzed the time course changes in the ESI-TOF mass spectra (Fig. 2 *B* and *C*). Since this racemization involves successive exchange of the six amine ligands **A** with piperidine, we had expected that we could observe all the mono- to penta-exchanged intermediates, **A5**, **A4**, **A3**, **A2**, and **A1**, during the reaction progress. However, only the di- and tetra-exchanged intermediates, **A4** and **A2**, were observed as a relatively intense peak. In particular, the tetra-exchanged intermediate $[LCo_3\mathbf{A}_2(pip)_4]^{3+}$ (=**A2**) was dominant, and its amount slowly decreased with the apparent half-life $t_{1/2(app)}$ of 18.2 min, whereas the di-exchanged intermediate $[LCo_3\mathbf{A}_4(pip)_2]^{3+}$ (=**A4**) rapidly disappeared at an early stage ($t_{1/2(app)}$ = 4.7 min).

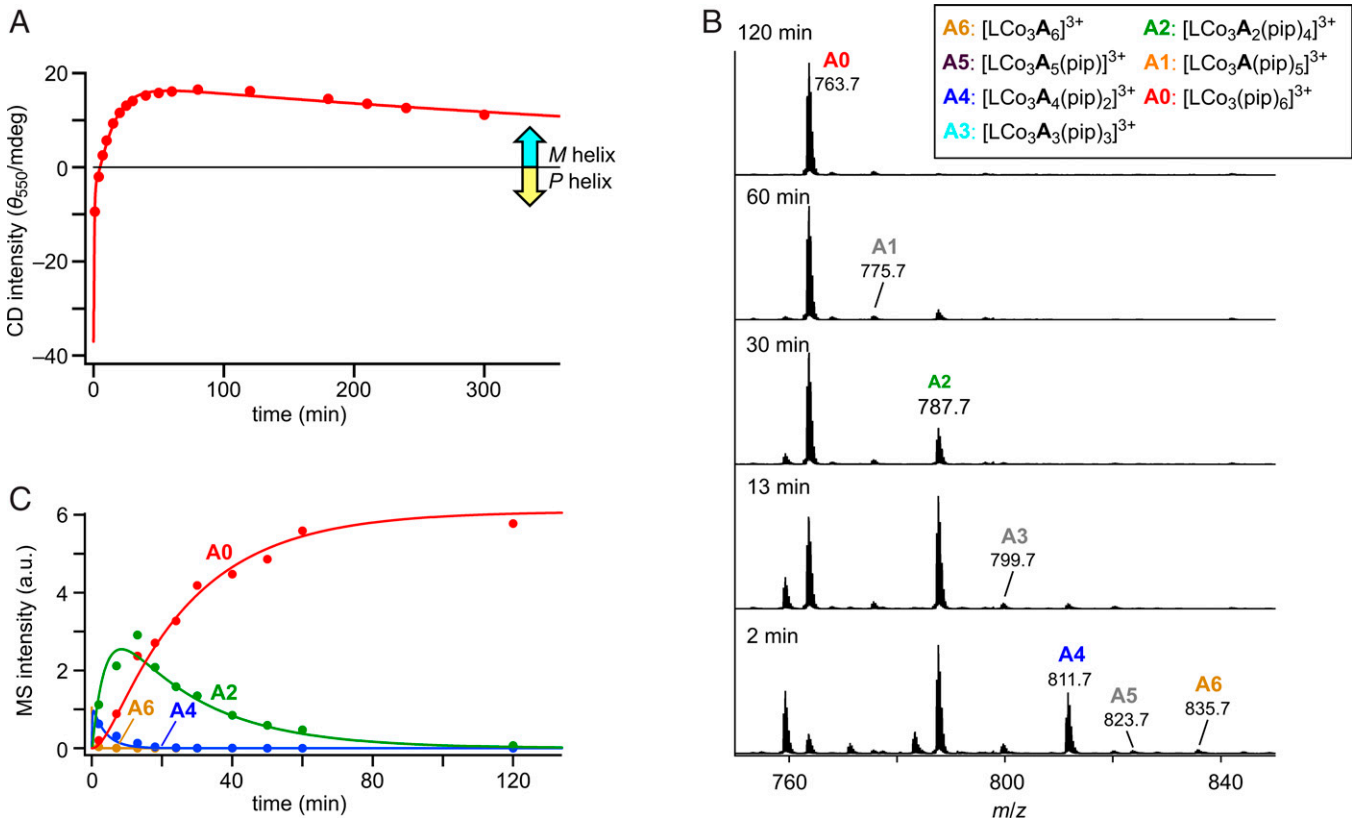

Fig. 2. Ligand exchange of $[LCo_3\mathbf{A}_6]^{3+}$ (=**A6**) with piperidine (120 equiv) in methanol at 298 K monitored by time course changes of the CD and mass spectra. (*A*) CD intensity at 550 nm. (*B*) ESI-TOF mass spectra; *m*/*z*, mass-to-charge ratio. (*C*) MS peak intensities of **A6**, **A4**, **A2**, and **A0**.

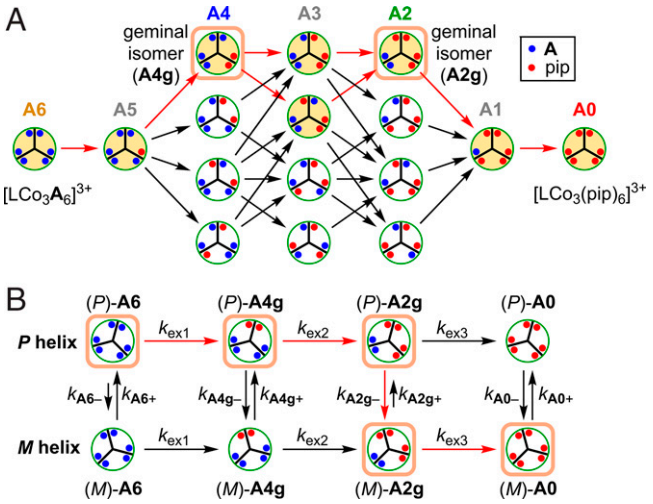

Fig. 3. Proposed mechanism of the transient chirality inversion observed during the racemization of $[LCo_3\mathbf{A}_6]^{3+}$ driven by ligand exchange. (*A*) Fourteen possible intermediates during the conversion of **A6** to **A0**. In this scheme, the *P*/*M* diastereomers are not differentiated. (*B*) Simplified three-step model of the ligand exchange with *P*/*M* helicity inversion. Red arrows represent the most probable paths of the conversion.

From a statistical point of view, this successive sixfold ligand exchange from **A6** to **A0** could give 14 possible intermediates ranging from mono- to penta-exchanged species including regioisomers and stereoisomers (Fig. 3*A*). However, the mono-, tri-, and penta-exchanged intermediates, **A5**, **A3**, and **A1**, were formed only in very small amounts. The absence of these species can be rationally explained by assuming that both of the two axial ligands at each cobalt(III) center are replaced with piperidine at virtually the same time. If this is the case, the plausible major pathways are limited to ones that involve only the geminal isomers of the intermediates, **A4g** and **A2g** (Fig. 3*A*). Thus, we simplified the sixfold ligand exchange as a three-step model, **A6** → **A4g** → **A2g** → **A0** with *P*/*M* equilibration (Fig. 3*B*). Each of the three steps was treated as a pseudo–first-order reaction because we used a large excess amount (120 equiv) of piperidine. For simplicity, we assumed that the rate constants for the *P* and *M* forms are the same for each of the three steps (k_{ex1}, k_{ex2}, and k_{ex3}).

We initially analyzed the time course changes of the peak intensities in the mass spectra (MS intensities hereafter) for **A6**, **A4g**, **A2g**, and **A0** (Fig. 2 *B* and *C* and *SI Appendix*, Fig. S6) without considering the *P*/*M* helicity of the $[LCo_3]^{3+}$ triple helix. The nonlinear curve fitting analysis yielded the rate constants of $k_{ex1} = 0.10\ s^{-1}$, $k_{ex2} = 4.5 \times 10^{-3}\ s^{-1}$, and $k_{ex3} = 6.7 \times 10^{-4}\ s^{-1}$, where k_{ex1}, k_{ex2}, and k_{ex3} are the pseudo–first-order rate constants for the three-step reaction (Figs. 2*C* and 3*B* and Table 1). The observed trend of $k_{ex1} > k_{ex2} > k_{ex3}$ can be explained by the increased number of bulky piperidine ligands; i.e., the ligand exchange at one site slows down the subsequent exchange reactions. This also indicated that the final-step conversion from **A2g** to **A0** is the rate-determining step of the overall three-step process.

Clearly, the observed transient chirality inversion (Fig. 2*A*) was caused by the *P*/*M* inversion at a later stage of the three-step conversion **A6** → **A4g** → **A2g** → **A0**. We analyzed the time course CD intensity changes assuming that each of the species can undergo the *P*/*M* helicity inversion with different rate constants (k_{S+} and k_{S-} for S = **A6**, **A4g**, **A2g**, and **A0**) while undergoing the ligand exchange with the rate constants (k_{ex1}, k_{ex2}, and k_{ex3}) determined by the above MS experiments (Fig. 3*B*). All the rate constants were optimized by a nonlinear least-squares regression of the overall experimental data of the CD and MS measurements (Table 1). The results unambiguously showed that the *P*/*M* helicity inversion becomes slower as more piperidine ligands are introduced. In particular, the final product, $[LCo_3(pip)_6]^{3+}$ (=**A0**), has the slowest rates for the *P*/*M* helicity inversion ($k_{\mathbf{A0}+} = k_{\mathbf{A0}-} = 1.2 \times 10^{-5}\ s^{-1}$), which is consistent with the observation that the CD intensity very slowly decayed after the complete ligand exchange (after 120 min; Fig. 2*A*). In addition, the equilibrium constants for the *P*/*M* helicity inversion, which are calculated as $K_S = k_{S+}/k_{S-}$ (S = **A6**, **A4g**, **A2g**, and **A0**), showed a unique trend that could explain the unprecedented transient chirality inversion. While there was almost no *P*/*M* preference for the di-exchanged intermediate **A4g** ($K_{\mathbf{A4g}} = k_{\mathbf{A4g}+}/k_{\mathbf{A4g}-} \sim 1.0$), the *P*/*M* equilibrium constant for the tetra-exchanged intermediate **A2g** was significantly lower than 1 ($K_{\mathbf{A2g}} = k_{\mathbf{A2g}+}/k_{\mathbf{A2g}-} = 0.16 \ll 1$). Consequently, the *M* form is more favorable for the tetra-exchanged intermediate **A2g**, whereas the *P* form is dominant in the starting complex **A6** ($K_{\mathbf{A6}} = k_{\mathbf{A6}+}/k_{\mathbf{A6}-} = 7.3 \gg 1$). Obviously, the helicity inversion occurred after four **A** ligands were replaced with piperidine. The most probable pathway, therefore, is that the starting complex **A6** underwent a fourfold ligand exchange to give the intermediate (*P*)-**A2g** while keeping the right-handed helicity, which then underwent a helicity inversion to give the left-handed (*M*)-**A2g**. This complex was then converted into the fully exchanged product (*M*)-**A0**, which very slowly underwent racemization (Fig. 3*B*).

Time Profiles of the Reverse Reaction. As already described, a unique transient chirality inversion was observed when $[LCo_3\mathbf{A}_6]^{3+}$ (=**A6**) loses the chiral ligands **A** upon the six-step ligand exchange with piperidine. In contrast, such a unique time response was not observed in the reverse reaction as we have already reported (54). Only a monotonic increase in the CD intensity was observed without showing a CD signal reversal when up to six molecules of chiral ligand **A** were introduced into the racemic $[LCo_3(pip)_6]^{3+}$ (=**A0**). However, we have found that this reverse reaction also showed a more distinct nonlinear feature when the amount of added **A** was increased from 12 to 120 equiv (Fig. 4*A* and *SI Appendix*, Fig. S8). During the first 30 min, the CD intensity showed almost no increase, although mono- to tetra-exchanged products (**A1**, **A2**, **A3**, **A4**,

Table 1. Rate constants for ligand exchange from A6 to A0 associated with helicity inversion in methanol at 298 K

Ligand exchange rates (s^{-1})*		*M*→*P* Helicity inversion rates (s^{-1})		*P*→*M* Helicity inversion rates (s^{-1})		*P*/*M* Equilibrium constant†	
k_{ex1}	0.10	$k_{\mathbf{A6}+}$	2.7×10^{-2}	$k_{\mathbf{A6}-}$	3.6×10^{-3}	$K_{\mathbf{A6}}$	7.3‡
k_{ex2}	4.5×10^{-3}	$k_{\mathbf{A4g}+}$	1.5×10^{-2}	$k_{\mathbf{A4g}-}$	1.5×10^{-2}	$K_{\mathbf{A4g}}$	0.95
k_{ex3}	6.7×10^{-4}	$k_{\mathbf{A2g}+}$	1.0×10^{-4}	$k_{\mathbf{A2g}-}$	6.4×10^{-4}	$K_{\mathbf{A2g}}$	0.16
		$k_{\mathbf{A0}+}$	1.2×10^{-5}	$k_{\mathbf{A0}-}$	1.2×10^{-5}	$K_{\mathbf{A0}}$	1§

*Pseudo–first-order rate constants. The rate constants k_{ex1}, k_{ex2}, and k_{ex3} for *P* and *M* forms are assumed to be the same for each of the ligand exchange steps.
†$K_S = k_{S+}/k_{S-}$ for S = **A6**, **A4g**, **A2g**, and **A0**.
‡$K_{\mathbf{A6}}$ (=$k_{\mathbf{A6}+}/k_{\mathbf{A6}-}$) was fixed at 7.3 based on the equilibrium ratio of (*P*)-**A6**:(*M*)-**A6** = 88:12.
§$K_{\mathbf{A0}}$ (=$k_{\mathbf{A0}+}/k_{\mathbf{A0}-}$) was fixed at 1 because (*P*)-**A0** and (*M*)-**A0** are enantiomers of each other.

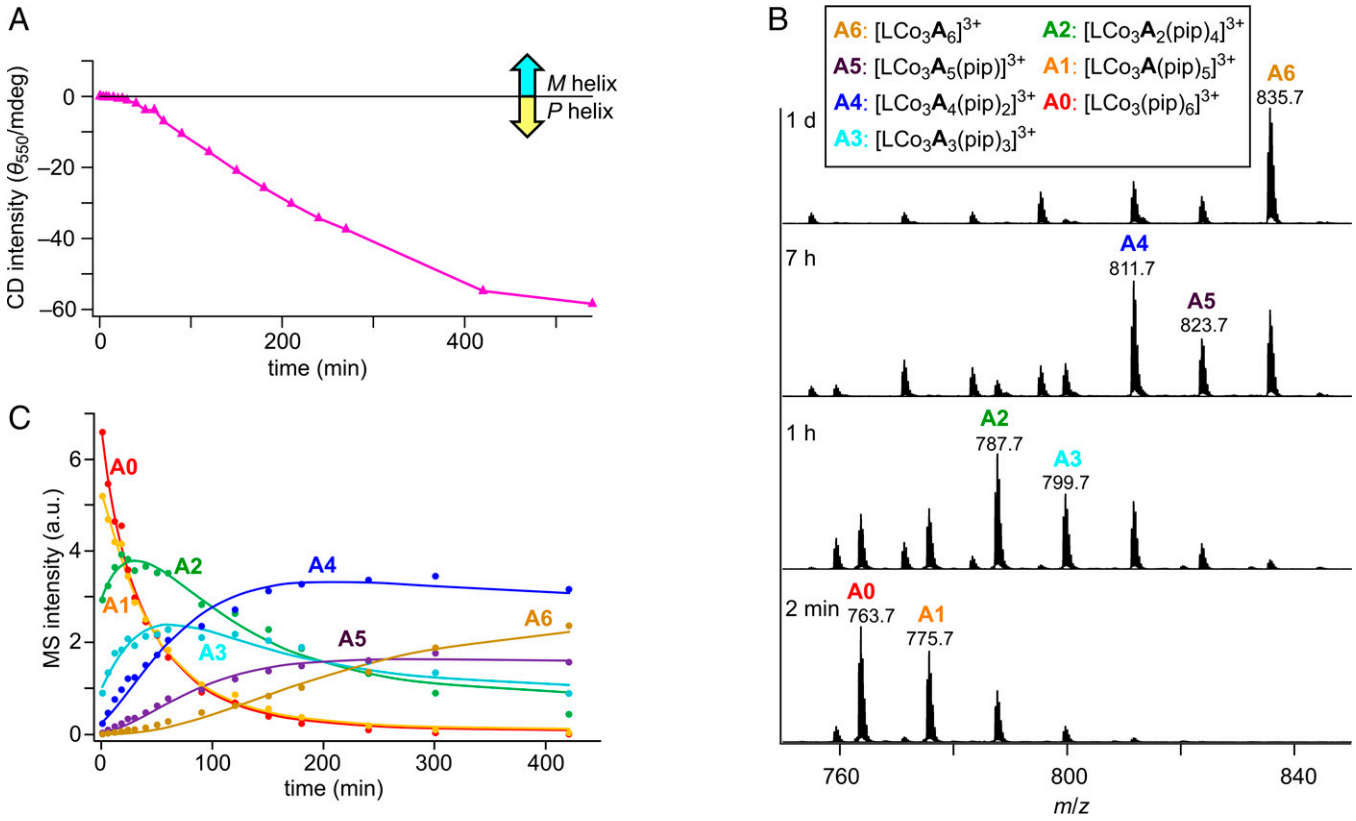

Fig. 4. Ligand exchange of $[LCo_3(pip)_6]^{3+}$ (=**A0**) with chiral amine **A** (120 equiv) in methanol at 298 K monitored by time course changes of the CD and mass spectra. (*A*) CD intensity at 550 nm. (*B*) ESI-TOF mass spectra. (*C*) MS peak intensities of **A0**, **A1**, **A2**, **A3**, **A4**, **A5**, and **A6**.

and **A5**) were observed with a significant intensity in the ESI-TOF mass spectra (Fig. 4 *B* and *C* and *SI Appendix*, Figs. S9–11). After this induction time of ∼30 min, the CD intensity monotonically increased for 500 min. During this reverse reaction, all the intermediates from the mono- to penta-exchanged species, **A1**, **A2**, **A3**, **A4**, and **A5**, were detected in the ESI-TOF mass spectra, which was in sharp contrast to the forward reaction in which only the di- and tetra-exchanged intermediates, **A4** and **A2**, were observed as dominating species (Fig. 2 *B* and *C*). In this reverse reaction, exchange of the six piperidine ligands in **A0** with the chiral ligands **A** probably took place in a statistically random manner via 14 intermediates (Fig. 3*A*). As the number of chiral ligands **A** increased, the negative CD signals simply increased without showing the transient chirality inversion.

As already discussed, the amount of the chiral amine **A**, 12 or 120 equiv, had a significant influence on the nonlinear feature of the time response in the reverse reaction starting from $[LCo_3(pip)_6]^{3+}$ (=**A0**). In contrast, the amount of the added piperidine did not significantly affect the unique time profile of the forward reaction starting from $[LCo_3\mathbf{A}_6]^{3+}$ (=**A6**). We still observed a similar transient chirality inversion that shows a CD signal inversion followed by a decay, even when the amount of piperidine was reduced from 120 to 12 equiv (*SI Appendix*, Figs. S12 and S13). This may be ascribed to the higher binding affinity of piperidine to the $[LCo_3]^{3+}$ triple helix than chiral amine **A**. In the forward reaction with 120 equiv of piperidine, more than 99% of the coordinating amine **A** was exchanged with piperidine at equilibrium, which was estimated from the time course analysis of the MS intensities (Fig. 2*C*). In contrast, a similar analysis for the reverse reaction with 120 equiv of **A** indicated that only 78% of the coordinating piperidine was exchanged with the chiral amine **A**. A significant amount of the intermediates **A2**, **A3**, **A4**, and **A5** still remained even at equilibrium (Fig. 4*C*). In order to quantitatively discuss the relative binding affinity of the amines, we defined the averaged equilibrium constant $K_{ex(av)}$ for the amine exchange between the chiral amine **A** and piperidine as

$$\boldsymbol{Co}\text{–}\mathbf{A} + \text{pip} \overset{K_{ex(av)}}{\rightleftarrows} \boldsymbol{Co}\text{–pip} + \mathbf{A},$$

where ***Co*-A** and ***Co*-pip** denote **A** and piperidine that are coordinating to the cobalt(III) centers, respectively. The $K_{ex(av)}$ was determined to be 6.9 from the estimated mole fractions of **A0** to **A6** at equilibrium in the reverse reaction, confirming that piperidine can more strongly coordinate to the cobalt(III) centers in the $[LCo_3]^{3+}$ triple helix than the chiral amine **A**.

Hysteretic Cycle in the Forward and Reverse Reactions. Based on the time dependence of the CD intensity, we found that the *M* helicity appeared only in the forward reaction **A6** → **A0** during the forward and reverse ligand exchanges between **A** and piperidine (Fig. 5*A*). Obviously, these forward and reverse reactions constitute a hysteretic cycle originating from the nonlinear feature of the six-step reactions. In fact, linearity is a feature originating from non–first-order reactions. In an ideal one-step first-order reaction X → Y, a physical quantity always changes in proportion to the reaction progress, which is defined as $[Y]/([X]_{initial})$, thus yielding a linear feature (Fig. 5*B*). In contrast, a two-step reaction described as XX → XY → YY does not necessarily show such a linear feature, particularly when the reaction proceeds in a stepwise manner ($k_1 \geq k_2$; Fig. 5*C*). Since the present system $[LCo_3X_6]^{3+}$ undergoes a six-step reaction, plots of the CD intensity vs. the reaction progress would give a nonlinear feature, which could well explain the unique hysteretic cycle.

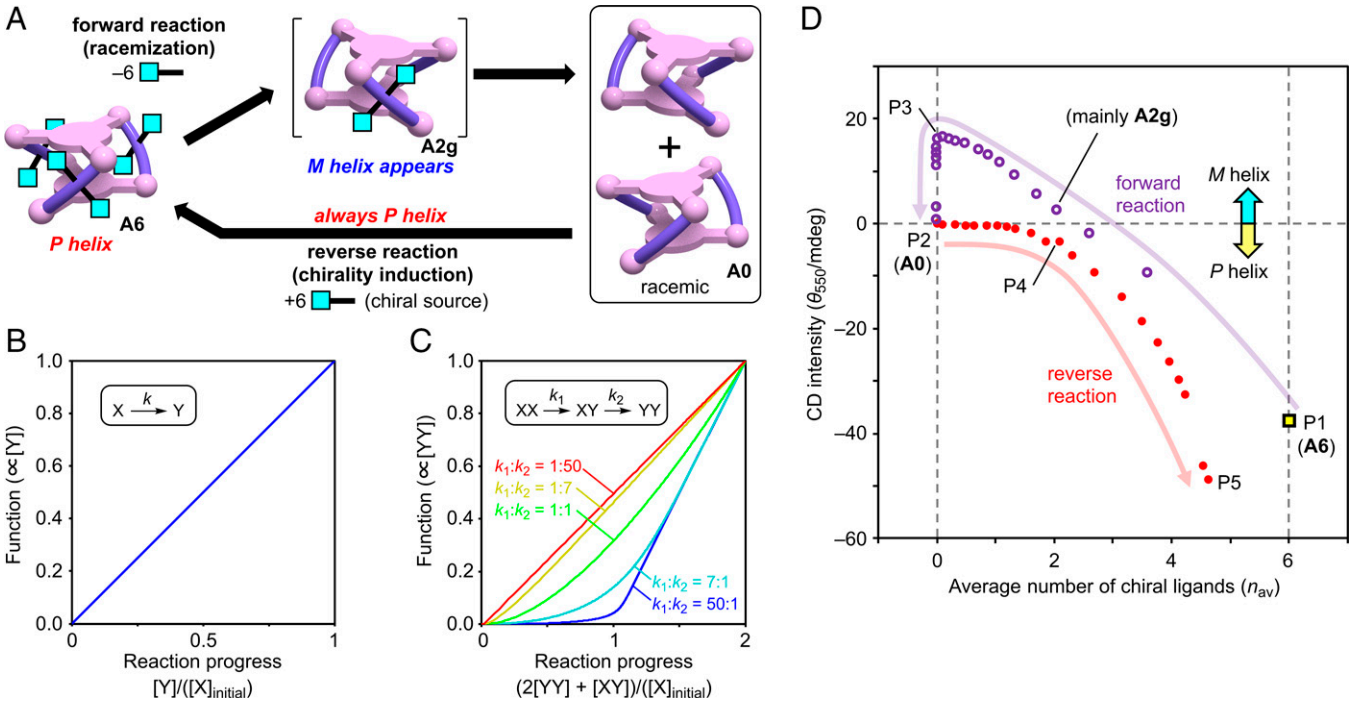

Fig. 5. Hysteretic cycle originating from the nonlinearity of the reactions. (*A*) The hysteretic cycle of the conversions of **A6** → **A0** and **A0** → **A6**. The *M* isomer appears only in the forward reaction. (*B*) Linearity of an ideal first-order reaction, X → Y. The function (proportional to [Y]) plotted versus reaction progress, which is defined as $[Y]/([X]_{initial})$, always shows a straight line. (*C*) Linearity of an ideal two-step reaction, XX → XY → YY. The function (proportional to [YY]) plotted versus the reaction progress, which is defined as the average number of Y, $(2[YY] + [XY])/([XX]_{initial})$, shows a significant nonlinearity when $k_1 \geq k_2$. (*D*) The plots of the CD intensity θ_{550} versus the average number of chiral amine ligands n_{av} throughout the reaction progress for the conversions of **A6** → **A0** and **A0** → **A6** in this study.

Thus, we defined the parameter n_{av}, which is the average number of chiral amine ligands **A** in $[LCo_3\mathbf{A}_n(pip)_{(6-n)}]^{3+}$ (**A0**, **A1**, … **A6**) at a given time, to describe the overall reaction progress. We made a plot of the CD intensity at 550 nm (θ_{550} in mdeg) versus n_{av} to analyze the linearity of the forward and reverse ligand exchanges (Fig. 5*D*). In this n_{av}–θ_{550} plot, the pure $[LCo_3\mathbf{A}_6]^{3+}$ (=**A6**) and $[LCo_3(pip)_6]^{3+}$ (=**A0**) are situated at the points P1 (n_{av}, θ_{550}) = (6, –35) and P2 (0, 0), respectively.

In the forward reaction from **A6** to **A0**, n_{av} at a given time was determined by the time course changes in the mole fractions of all the major intermediates, **A6**, **A4g**, **A2g**, and **A0** (Fig. 2*C*). The observed data points (n_{av}, θ_{550}) moved from P1 to P2 as time proceeded in this n_{av}–θ_{550} plot (Fig. 5*D*). The trajectory of the points (n_{av}, θ_{550}) showed a distinct two-phase feature, P1 → P3 → P2, instead of a straight line corresponding to a linear relationship. In the first phase, the negative CD immediately decreased and turned positive with the reaction progress [i.e., from P1 (n_{av}, θ_{550}) = (6, –35) to P3 (0, +17)]. In the second phase, the positive CD decreased to P2 (0, 0) keeping $n_{av} \sim 0$. This two-phase trajectory well explains the two-step feature of the transient chirality inversion observed during the forward reaction.

The reverse reaction from **A0** to **A6** was also analyzed by using this n_{av}–θ_{550} plot. The n_{av} at a given time was determined by the mole fractions for all the intermediates, **A1**, **A2**, **A3**, **A4**, and **A5**, as well as **A0** and **A6**, which were estimated by simulating the time course changes of their MS peak intensities (Fig. 4*C* and *SI Appendix*, Fig. S11). Although a seemingly simple monotonic increase in θ_{550} was observed upon the exchange of the piperidine with the chiral ligand **A**, the n_{av}–θ_{550} plot showed a significant nonlinear feature (Fig. 5*D*). During an earlier stage of the reaction, the ligand exchange caused only a small change in the CD intensity θ_{550} [i.e., from P2 (n_{av}, θ_{550}) = (0, 0) to P4 (2.1, –3.5)]. This means that almost no helicity inversion occurred until two of the six piperidine ligands were replaced with the chiral ligand **A**. This is consistent with the fact that $[LCo_3(pip)_6]^{3+}$ (=**A0**) has the slowest helicity inversion rates ($k_{\mathbf{A0}+} = k_{\mathbf{A0}-} = 1.2 \times 10^{-5}$ s^{-1}) (Fig. 3*B* and Table 1). When the ligand exchange further proceeded ($n_{av} > 2.5$), the CD intensity rapidly increased from P4 (n_{av}, θ_{550}) = (2.1, –3.5) to P5 (4.6, –49). As the ligand exchange proceeds, the helicity inversion equilibrium of the $[LCo_3]^{3+}$ triple helix becomes faster due to the loss of the bulky piperidine ligands, and the *P* helicity becomes more favored when more **A** ligands were introduced. As a result, the *M* helicity appeared only in the forward reaction **A6** → **A0**, and hysteresis was observed during the erasing/writing cycle of the helicity in the cobalt(III) metallocryptand $[LCo_3X_6]^{3+}$ by decreasing/increasing the average number of chiral amine ligands, n_{av}, in the range between 0 and 6 (Fig. 5*A*).

Conclusion

The helical complex $[LCo_3X_6]^{3+}$ having six exchangeable ligands showed a unique time response, transient chirality inversion, during racemization. The starting *P* helix of $[LCo_3\mathbf{A}_6]^{3+}$ did not simply racemize in a monotonic fashion; the opposite *M* helix appeared during the stereomutation prior to the complete removal of the chiral source **A**, despite the absence of a reagent that could induce the *M* helix. Thus, the handedness of the helix changed from *P*-rich to *M*-rich, which then racemized to a *P*/*M* equimolar mixture. This overshooting profile of the time course change, i.e., sign inversion followed by a decay to zero, is quite similar to the damped oscillation observed in physics, such as classical mechanics and electromagnetism. Previously, a nontrivial time response has been observed only in complicated autocatalytic systems and in self-assembled systems. The present

$[LCo_3X_6]^{3+}$ system demonstrated that a transient chirality inversion can be observed on a unimolecular platform. One of the noteworthy features is that this transient chirality inversion was observed only in the forward reaction. The forward and reverse reactions proceeded in different pathways to make a hysteretic cycle. Moreover, the unique time course change in this system is easily observable on the timescale of minutes to hours, which would be potentially useful for time-dependent functional materials in human activities.

The development of a unimolecular system with such a nontrivial time response would enable time-programmable switches that can control the physical properties and chemical reactivities in a time-dependent manner. We believe that this result will provide an important insight into the science of autonomously driven materials. Further advanced materials with oscillating responses would be realized in combination with various types of reactions such as sequential reactions or autocatalytic reactions.

Materials and Methods

General. $[LCo_3A_6](OTf)_3$ and $[LCo_3(pip)_6](OTf)_3$ were synthesized according to the previous report (54). The reagents and solvents were purchased from commercial sources and used without further purification. The ^{1}H NMR spectra were recorded on a JEOL JNM-ECS 400 (400 MHz). Chemical shifts were referenced with respect to the solvent residual peak (3.31 ppm for CD_2HOD; 1.94 ppm for CD_2HCN). The ESI-TOF MS measurements were performed on a Bruker Daltonics micrOTOF II spectrometer. The CD spectra were recorded on a JASCO J-1500 spectropolarimeter at 298 K.

Determination of Rate Constants.

Step 1: Determination of rate constants for the three-step ligand exchange A6 → A4g → A2g → A0. Experimentally obtained time dependence of MS intensities, $I_{obs,S,i}$ (S = **A6**, **A4**, **A2**, and **A0**; *i*th data at time t_i out of all the measured points n_{MS}; t_i is the time after the reaction started), was used to determine the time course change of the mole fractions. The corresponding simulated MS intensities for these species, $I_{sim,S,i}$, are given as the following equation:

$$I_{sim,S,i} = A_S \bullet R_S(t_i),$$

where $R_S(t)$ is the mole fraction of each species (S = **A6**, **A4g**, **A2g**, and **A0**) at the given time t, and A_S is a constant. The time dependence of the mole fractions, $R_S(t)$, was simulated by numerical integration methods with the step of dt = 1 s based on the given rate constants k_{ex1}, k_{ex2}, and k_{ex3}, assuming that each of the three-step ligand exchange reactions of **A6** → **A4g** → **A2g** → **A0** is irreversible pseudo–first-order and that the *P* and *M* isomers of each species (**A6**, **A4g**, and **A2g**) have the same rate constants for each step. The variables of k_{ex1}, k_{ex2}, k_{ex3}, and A_S (S = **A6**, **A4g**, **A2g**, and **A0**) were optimized by a least-squares regression to minimize the residual r_{MS} defined by the following equation:

$$r_{MS} = \sum_S \left(\sum_{i=1}^{n_{MS}} (I_{obs,S,i} - I_{sim,S,i})^2 \right) = \sum_S \left(\sum_{i=1}^{n_{MS}} (I_{obs,S,i} - A_S \bullet R_S(t_i))^2 \right),$$

using the Solver Add-In in Microsoft Excel.

Step 2: Determination of rate constants for the P/M isomerization for A6, A4g, A2g, and A0. The experimentally obtained time dependence of the CD intensities, $\theta_{obs,j}$ (*j*th data at time t_j out of all the measured points n_{CD}; t_j is the time after the reaction started), was used to analyze the time course change of the CD intensities. The corresponding simulated CD intensities $\theta_{sim,j}$ are given as the following equation:

$$\theta_{sim,j} = \sum_S B_S \bullet R_S(t_j),$$

where $R_S(t)$ is the mole fraction of each species [S = (*P*)-**A6**, (*P*)-**A4g**, (*P*)-**A2g**, (*P*)-**A0**, (*M*)-**A6**, (*M*)-**A4g**, (*M*)-**A2g**, (*M*)-**A0**] at the given time t, and B_S is a constant. For simplicity, $|B_S|$ for all species is assumed to be the same as B and their signs are only dependent on the helicity as follows:

$$B_{(P)\text{-}\mathbf{A6}} = B_{(P)\text{-}\mathbf{A4g}} = B_{(P)\text{-}\mathbf{A2g}} = B_{(P)\text{-}\mathbf{A0}} = B,$$
$$B_{(M)\text{-}\mathbf{A6}} = B_{(M)\text{-}\mathbf{A4g}} = B_{(M)\text{-}\mathbf{A2g}} = B_{(M)\text{-}\mathbf{A0}} = -B,$$

because the CD intensities of each species are mostly governed by the triple-helical structures of the $[LCo_3(amine)_6]^{3+}$ regardless of the coordinating amine ligands.

The time dependence of the mole fractions, $R_S(t)$, was simulated by numerical integration methods with the step of dt = 1 s based on the given rate constants k_{ex1}, k_{ex2}, and k_{ex3}, assuming that each of the three-step ligand exchange reactions of **A6** → **A4g** → **A2g** → **A0** is irreversible and that the *P* and *M* isomers of each species (**A6**, **A4g**, and **A2g**) have the same rate constants for each step, as described for the previously mentioned step 1. The variables of k_{A6+}, k_{A6-}, k_{A4g+}, k_{A4g-}, k_{A2g+}, k_{A2g-}, k_{A0+}, k_{A0-}, and B were optimized by a further simultaneous refinement of k_{ex1}, k_{ex2}, k_{ex3}, and A_S (S = **A6**, **A4g**, **A2g**, and **A0**) by a least-squares regression to minimize the residual r defined as the following equation:

$$r = w_{MS} \bullet r_{MS} + w_{CD} \bullet r_{CD},$$
$$r_{CD} = \sum_{j=1}^{n_{CD}} (\theta_{obs,j} - \theta_{sim,j})^2 = \sum_{j=1}^{n_{CD}} \left(\theta_{obs,j} - \sum_S B_S R_S(t_j) \right)^2,$$

where w_{MS} and w_{CD} are the weights of the MS and CD measurements, respectively, using the Solver Add-In in Microsoft Excel, while applying the following constraints:

$$k_{A6+} : k_{A6-} = 88 : 12,$$
$$k_{A0+} = k_{A0-},$$

based on the experimentally determined *P*/*M* ratio of **A6** at equilibrium and that (*P*)-**A0** and (*M*)-**A0** constitute an enantiomer pair.

Step 3: Determination of rate constants for six-step ligand exchange in the reverse reaction. The experimentally obtained time dependence of MS intensities, $I_{obs,S,i}$ (S = **A0**, **A1**, **A2**, **A3**, **A4**, **A5**, and **A6**; *i*th data at time t_i out of all the measured points n_{MS}; t_i is the time after the reaction started), was used to determine the time course change in the mole fractions. The corresponding simulated MS intensities $I_{sim,S,i}$ for these species are given as the following equation:

$$I_{sim,S,i} = A_S \bullet R_S(t_i),$$

where $R_S(t)$ is the mole fraction of each species (S = **A0**, **A1**, **A2**, **A3**, **A4**, **A5**, and **A6**) at the given time t and A_S is a constant. The time dependence of the mole fractions, $R_S(t)$, was simulated by numerical integration methods with the step of dt = 0.1 min based on the given rate constants k'_{ex1+}, k'_{ex1-}, k'_{ex2+}, k'_{ex2-}, k'_{ex3+}, k'_{ex3-}, k'_{ex4+}, k'_{ex4-}, k'_{ex5+}, k'_{ex5-}, k'_{ex6+}, and k'_{ex6-} assuming that each of the six-step ligand exchange reactions of **A0** → **A1** → **A2** → **A3** → **A4** → **A5** → **A6** is reversible and that all the diastereomers of each species have the same rate constants. The variables of k'_{ex1+}, k'_{ex1-}, k'_{ex2+}, k'_{ex2-}, k'_{ex3+}, k'_{ex3-}, k'_{ex4+}, k'_{ex4-}, k'_{ex5+}, k'_{ex5-}, k'_{ex6+}, k'_{ex6-}, and A_S (S = **A0**, **A1**, **A2**, **A3**, **A4**, **A5**, and **A6**) were optimized by the least-squares regression to minimize the residual r_{MS} defined by the following equation:

$$r_{MS} = \sum_S \left(\sum_{i=1}^{n_{MS}} (I_{obs,S,i} - I_{sim,S,i})^2 \right) = \sum_S \left(\sum_{i=1}^{n_{MS}} (I_{obs,S,i} - A_S \bullet R_S(t_i))^2 \right),$$

using the Solver Add-In in Microsoft Excel.

Data Availability. All study data are included in the article and/or *SI Appendix*.

ACKNOWLEDGMENTS. This work was supported by Japan Society for the Promotion of Science (KAKENHI Grants JP16H06510 [Coordination Asymmetry], JP26288022, JP18H03913, JP20K21206, and JP21H05477), The Iwatani Naoji Foundation, The Asahi Glass Foundation, and the World Premier International Research Initiative, Ministry of Education, Culture, Sports, Science and Technology, Japan.

1. A. J. McConnell, C. S. Wood, P. P. Neelakandan, J. R. Nitschke, Stimuli-responsive metal-ligand assemblies. *Chem. Rev.* **115**, 7729–7793 (2015).
2. D.-H. Qu, Q.-C. Wang, Q.-W. Zhang, X. Ma, H. Tian, Photoresponsive host-guest functional systems. *Chem. Rev.* **115**, 7543–7588 (2015).
3. S. J. Wezenberg, Light-switchable metal-organic cages. *Chem. Lett.* **49**, 609–615 (2020).
4. P. L. Boulas, M. Gómez-Kaifer, L. Echegoyen, Electrochemistry of supramolecular systems. *Angew. Chem. Int. Ed.* **37**, 216–247 (1998).
5. A. K.-W. Chan, W. H. Lam, Y. Tanaka, K. M.-C. Wong, V. W.-W. Yam, Multiaddressable molecular rectangles with reversible host-guest interactions: Modulation of pH-controlled guest release and capture. *Proc. Natl. Acad. Sci. U.S.A.* **112**, 690–695 (2015).
6. H. Landolt, Ueber die Zeitdauer der Reaction zwischen Jodsäure und schwefliger Säure. *Ber. Dtsch. Chem. Ges.* **19**, 1317–1365 (1886).
7. A. P. Oliveira, R. B. Faria, The chlorate-iodine clock reaction. *J. Am. Chem. Soc.* **127**, 18022–18023 (2005).
8. A. M. Zhabotinsky, Belousov-Zhabotinsky reaction. *Scholarpedia* **2**, 1435 (2007).
9. J. Ross, M. O. Vlad, Nonlinear kinetics and new approaches to complex reaction mechanisms. *Annu. Rev. Phys. Chem.* **50**, 51–78 (1999).
10. A. F. Taylor, Mechanism and phenomenology of an oscillating chemical reaction. *Prog. React. Kinet. Mech.* **27**, 247–325 (2002).
11. A. T. Winfree, Oscillating systems. On emerging coherence. *Science* **298**, 2336–2337 (2002).

12. L. Györgyi, T. Turányi, R. J. Field, Mechanistic details of the oscillatory Belousov-Zhabotinskii reaction. *J. Phys. Chem.* **94**, 7162–7170 (1990).
13. I. R. Epstein, K. Showalter, Nonlinear chemical dynamics: Oscillations, patterns, and chaos. *J. Phys. Chem.* **100**, 13132–13147 (1996).
14. M. Orbán, K. Kurin-Csörgei, I. R. Epstein, pH-regulated chemical oscillators. *Acc. Chem. Res.* **48**, 593–601 (2015).
15. R. Yoshida, T. Ueki, Evolution of self-oscillating polymer gels as autonomous polymer systems. *NPG Asia Mater.* **6**, e107 (2014).
16. G. Wang *et al.*, The fabrication of a supra-amphiphile for dissipative self-assembly. *Chem. Sci.* **7**, 1151–1155 (2016).
17. M. Onoda, T. Ueki, R. Tamate, M. Shibayama, R. Yoshida, Amoeba-like self-oscillating polymeric fluids with autonomous sol-gel transition. *Nat. Commun.* **8**, 15862 (2017).
18. T. Yoshizawa *et al.*, Fabrication of self-oscillating micelles with a built-in oxidizing agent. *Angew. Chem. Int. Ed.* **59**, 3871–3875 (2020).
19. Q. Shao, S. Zhang, Z. Hu, Y. Zhou, Multimode self-oscillating vesicle transformers. *Angew. Chem. Int. Ed.* **59**, 17125–17129 (2020).
20. E. Mattia, S. Otto, Supramolecular systems chemistry. *Nat. Nanotechnol.* **10**, 111–119 (2015).
21. G. Ashkenasy, T. M. Hermans, S. Otto, A. F. Taylor, Systems chemistry. *Chem. Soc. Rev.* **46**, 2543–2554 (2017).
22. S. A. P. van Rossum, M. Tena-Solsona, J. H. van Esch, R. Eelkema, J. Boekhoven, Dissipative out-of-equilibrium assembly of man-made supramolecular materials. *Chem. Soc. Rev.* **46**, 5519–5535 (2017).
23. M. Tena-Solsona *et al.*, Non-equilibrium dissipative supramolecular materials with a tunable lifetime. *Nat. Commun.* **8**, 15895 (2017).
24. G. Ragazzon, L. J. Prins, Energy consumption in chemical fuel-driven self-assembly. *Nat. Nanotechnol.* **13**, 882–889 (2018).
25. B. Rieß, R. K. Grötsch, J. Boekhoven, The design of dissipative molecular assemblies driven by chemical reaction cycles. *Chem* **6**, 552–578 (2020).
26. A. Mishra *et al.*, Biomimetic temporal self-assembly via fuel-driven controlled supramolecular polymerization. *Nat. Commun.* **9**, 1295 (2018).
27. J. Boekhoven, W. E. Hendriksen, G. J. M. Koper, R. Eelkema, J. H. van Esch, Transient assembly of active materials fueled by a chemical reaction. *Science* **349**, 1075–1079 (2015).
28. S. Maiti, I. Fortunati, C. Ferrante, P. Scrimin, L. J. Prins, Dissipative self-assembly of vesicular nanoreactors. *Nat. Chem.* **8**, 725–731 (2016).
29. L. S. Kariyawasam, C. S. Hartley, Dissipative assembly of aqueous carboxylic acid anhydrides fueled by carbodiimides. *J. Am. Chem. Soc.* **139**, 11949–11955 (2017).
30. A. Ghosh, I. Paul, M. Schmittel, Multitasking with chemical fuel: Dissipative formation of a pseudorotaxane rotor from five distinct components. *J. Am. Chem. Soc.* **143**, 5319–5323 (2021).
31. T. Ikegami, Y. Kageyama, K. Obara, S. Takeda, Dissipative and autonomous square-wave self-oscillation of a macroscopic hybrid self-assembly under continuous light irradiation. *Angew. Chem. Int. Ed.* **55**, 8239–8243 (2016).
32. J. Leira-Iglesias, A. Tassoni, T. Adachi, M. Stich, T. M. Hermans, Oscillations, travelling fronts and patterns in a supramolecular system. *Nat. Nanotechnol.* **13**, 1021–1027 (2018).
33. S. Dhiman, S. J. George, Temporally controlled supramolecular polymerization. *Bull. Chem. Soc. Jpn.* **91**, 687–699 (2018).
34. J. Matern, Y. Dorca, L. Sánchez, G. Fernández, Revising complex supramolecular polymerization under kinetic and thermodynamic control. *Angew. Chem. Int. Ed.* **58**, 16730–16740 (2019).
35. S. Ogi, K. Sugiyasu, S. Manna, S. Samitsu, M. Takeuchi, Living supramolecular polymerization realized through a biomimetic approach. *Nat. Chem.* **6**, 188–195 (2014).
36. S. Ogi, T. Fukui, M. L. Jue, M. Takeuchi, K. Sugiyasu, Kinetic control over pathway complexity in supramolecular polymerization through modulating the energy landscape by rational molecular design. *Angew. Chem. Int. Ed.* **53**, 14363–14367 (2014).
37. T. Fukui, M. Takeuchi, K. Sugiyasu, Autocatalytic time-dependent evolution of metastable two-component supramolecular assemblies to self-sorted or coassembled state. *Sci. Rep.* **7**, 2425 (2017).
38. T. Fukui, N. Sasaki, M. Takeuchi, K. Sugiyasu, Living supramolecular polymerization based on reversible deactivation of a monomer by using a 'dummy' monomer. *Chem. Sci.* **10**, 6770–6776 (2019).
39. Q. Wan, W.-P. To, X. Chang, C.-M. Che, Controlled synthesis of Pd^{II} and Pt^{II} supramolecular copolymer with sequential multiblock and amplified phosphorescence. *Chem* **6**, 945–967 (2020).
40. S. Sarkar, A. Sarkar, S. J. George, Stereoselective seed-induced living supramolecular polymerization. *Angew. Chem. Int. Ed.* **59**, 19841–19845 (2020).
41. J. Matern, N. Bäumer, G. Fernández, Unraveling halogen effects in supramolecular polymerization. *J. Am. Chem. Soc.* **143**, 7164–7175 (2021).
42. I. Robayo-Molina, A. F. Molina-Osorio, L. Guinane, S. A. M. Tofail, M. D. Scanlon, Pathway complexity in supramolecular porphyrin self-assembly at an immiscible liquid-liquid interface. *J. Am. Chem. Soc.* **143**, 9060–9069 (2021).
43. S. Ogi, V. Stepanenko, K. Sugiyasu, M. Takeuchi, F. Würthner, Mechanism of self-assembly process and seeded supramolecular polymerization of perylene bisimide organogelator. *J. Am. Chem. Soc.* **137**, 3300–3307 (2015).
44. S. Lee *et al.*, Finely controlled circularly polarized luminescence of a mechano-responsive supramolecular polymer. *Angew. Chem. Int. Ed.* **58**, 18878–18882 (2019).
45. I. Helmers, G. Ghosh, R. Q. Albuquerque, G. Fernández, Pathway and length control of supramolecular polymers in aqueous media via a hydrogen bonding lock. *Angew. Chem. Int. Ed.* **60**, 4368–4376 (2021).
46. F. Xu *et al.*, From photoinduced supramolecular polymerization to responsive organogels. *J. Am. Chem. Soc.* **143**, 5990–5997 (2021).
47. P. A. Korevaar *et al.*, Pathway complexity in supramolecular polymerization. *Nature* **481**, 492–496 (2012).
48. F. Aparicio *et al.*, Inversion of supramolecular helicity in oligo-*p*-phenylene-based supramolecular polymers: Influence of molecular atropisomerism. *Angew. Chem. Int. Ed.* **53**, 1373–1377 (2014).
49. M. Shigeno, Y. Kushida, M. Yamaguchi, Heating/cooling stimulus induces three-state molecular switching of pseudoenantiomeric aminomethylenehelicene oligomers: Reversible nonequilibrium thermodynamic processes. *J. Am. Chem. Soc.* **136**, 7972–7980 (2014).
50. B. Kemper *et al.*, Kinetically controlled stepwise self-assembly of Au^{I}-metallopeptides in water. *J. Am. Chem. Soc.* **140**, 534–537 (2018).
51. H. Choi *et al.*, Kinetically controlled Ag^{+}-coordinated chiral supramolecular polymerization accompanying a helical inversion. *Chem. Sci.* **11**, 721–730 (2020).
52. S. Akine, M. Miyashita, T. Nabeshima, A metallo-molecular cage that can close the apertures with coordination bonds. *J. Am. Chem. Soc.* **139**, 4631–4634 (2017).
53. S. Akine, M. Miyashita, T. Nabeshima, A closed metallomolecular cage that can open its aperture by disulfide exchange. *Chem. Eur. J.* **25**, 1432–1435 (2019).
54. Y. Sakata, S. Chiba, M. Miyashita, T. Nabeshima, S. Akine, Ligand exchange strategy for tuning of helicity inversion speeds of dynamic helical tri(saloph) metallocryptands. *Chem. Eur. J.* **25**, 2962–2966 (2019).
55. Y. Sakata, C. Murata, S. Akine, Anion-capped metallohost allows extremely slow guest uptake and on-demand acceleration of guest exchange. *Nat. Commun.* **8**, 16005 (2017).
56. Y. Sakata, M. Tamiya, M. Okada, S. Akine, Switching of *recognition first* and *reaction first* mechanisms in host-guest binding associated with chemical reactions. *J. Am. Chem. Soc.* **141**, 15597–15604 (2019).
57. Y. Sakata, M. Okada, M. Tamiya, S. Akine, Post-metalation modification of a macrocyclic dicobalt(III) metallohost by site-selective ligand exchange for guest recognition control. *Chem. Eur. J.* **26**, 7595–7601 (2020).
58. Y. Sakata, M. Okada, S. Akine, Guest recognition control accompanied by stepwise gate closing and opening of a macrocyclic metallohost. *Chem. Eur. J.* **27**, 2284–2288 (2021).
59. S. Akine, Control of guest binding behavior of metal-containing host molecules by ligand exchange. *Dalton Trans.* **50**, 4429–4444 (2021).
60. S. Akine, M. Miyashita, S. Piao, T. Nabeshima, Perfect encapsulation of a guanidinium ion in a helical trinickel(II) metallocryptand for efficient regulation of the helix inversion rate. *Inorg. Chem. Front.* **1**, 53–57 (2014).
61. S. Akine, M. Miyashita, T. Nabeshima, Enhancement of alkali metal ion recognition by metalation of a tris(saloph) cryptand having benzene rings at the bridgeheads. *Inorg. Chem.* **60**, 12961–12971 (2021).